A High-Voltage Lithium-Metal Batteries Electrolyte Based on Fully-Methylated Pivalonitrile

Shaopeng Li,[a] Shan Fang,[a] Zhiwei Li,[a] Weiyi Chen,[a] Hui Dou,[a] and Xiaogang Zhang*[a]

Nitrile-based electrolytes with high-voltage have emerged as attractive candidates for high energy intensive lithium-metal batteries (LMBs). But they are still hampered by the inherent instability of reductive lithium anodes. Herein, we propose a fully methylated pivalonitrile (PN) as a stable electrolyte solvent for LMBs. This nitrile-based electrolyte achieves a wide electrochemical window and desired compatibility towards LMB, the assembled Li∣∣Li symmetric cells can achieve satisfying electrochemical performance with low overpotential and high durability (500 h). The uniform and dense Li deposition investigated by operando monitoring during the Li metal plating process reveals the high Coulombic efficiency (CE) and long-term durability. Furthermore, the full cell coupled with LiNi$_{0.6}$Mn$_{0.2}$Co$_{0.2}$O$_2$ using this optimized electrolyte displays enhanced capacity retention (75.3% after 300 cycles at 1 C) together with better stability and less CO$_2$ gas production. This study provides new insights in the development of high safety electrolytes and promotes the practical application of high-voltage lithium-metal batteries.

Introduction

Rechargeable lithium-ion batteries (LIBs) have enabled great progress in portable electronics and automotive applications owing to their high-energy output and satisfactory lifetime.[1–4] The most used commercial materials (graphite anodes) have reached their theoretical capacities (372 mAh g^{-1}), limiting the energy density of LIBs (~250 Wh kg^{-1}).[5] To satisfy the growing demand for high-energy-density, tremendous efforts have been made to explore new anode materials. Notably, the re-prospered Li metal stands out among various electrode materials by virtue of its high theoretical specific capacity (3860 mAh g^{-1}) and the lowest reduction potential (-3.04 V versus SHE).[6,7] Nevertheless, the Li metal anode is still hindered by uncontrollable dendrite growth and poor cyclability in practical application.[8–10]

Currently, liquid electrolytes based on carbonates and ethers are extensively used in lithium metal batteries, which suffers from security hazards by low Coulombic efficiency (CE) and incompatibility towards both lithium anodes and high-voltage cathodes.[11] More importantly, the metallic Li can react with lots of organic solvents and lithium salts for the sack of its spontaneous brisk reactivity, thus it is easy to form a heterogeneity solid-electrolyte interphase (SEI) layer with low mechanical/chemical stability and ionic conductivity,[12–14] which leads to inhomogeneous Li-ion flux and growth of dendrites,[15,16] Additionally, When applying Ni-rich Li-[Ni$_x$Co$_y$Mn$_z$]O$_2$ (NCM) as cathode materials in lithium metal batteries, undesirable HF resulting from the reaction of lithium with trace water will attack the alkaline cathode material and lead to the dissolution of transition metal elements (such as Ni, Co, Mn).[17,18]

To overcome the above limitations, much efforts have been devoted to develop electrolytes with high interfacial stability of high-voltage cathodes in lithium metal batteries,[19–25] including fluorinated electrolytes,[26,27] deep eutectic solvent electrolytes,[28] sulfone-type electrolytes,[29,30] amide-type electrolytes,[31] and nitrile-type electrolytes.[32–35] Among them, nitrile-type electrolyte (such as succinonitrile, adiponitrile) with high chemical stability and oxidation resistance has been widely employed to improve the cycling performance and stability of cathodes at high voltage. The strong complexation of nitriles can restrain the oxidation reactions of the electrolyte on the surface of Ni-rich cathode and remove trace amounts of water from the electrolyte and HF hydrolyzed from lithium salt. However, the development of nitrile-type electrolytes remains challenging in view of poor compatibility with Li metal.[36]

Herein, we propose an aprotic solvent pivalonitrile (PN) as a stable electrolyte solvent for LMBs. Because the active α-H atoms are all replaced with methyl groups, the stability of the solvent can be further enhanced and inhibits the formation of free cyanide. The LiTFSI–FEC–PN [TFP, 1 M LiTFSI in FEC/PN (2:3, v%)] electrolyte shows excellent ionic transport characteristics caused by a high lithium-ion transference number (t_{Li}^+) of 0.58. As a consequence, this optimal electrolyte exhibits promising ionic conductivity (11.53 mS cm^{-1}) and low viscosity (3.47 mPa s), enhancing the stability of the electrode/electrolyte interface, improving Li metal plating/stripping performance, as well as significantly suppressed gas releasing. An ascensive Coulombic efficiency of 96.2% in Li∣∣Cu asymmetric cell can be achieved by using TFP electrolyte at a current density of 1 mA cm^{-2}. When coupling with a LiNi$_{0.6}$Mn$_{0.2}$Co$_{0.2}$O$_2$ (NCM622) cathode, excellent cycling stability can be demonstrated at 1 C, together with a wide voltage range of 2.8–4.5 V (vs. Li/Li$^+$).

[a] S. Li, S. Fang, Z. Li, W. Chen, Prof. H. Dou, Prof. X. Zhang
Jiangsu Key Laboratory of Electrochemical Energy Storage Technologies
College of Material Science and Engineering
Nanjing University of Aeronautics and Astronautics
Nanjing, 210016, China
E-mail: azhangxg@nuaa.edu.cn

Batteries & Supercaps

Research Article
doi.org/10.1002/batt.202100416

Chemistry Europe
European Chemical
Societies Publishing

Furthermore, operando monitoring and differential electro-chemical mass spectrometry (DEMS) provide a deep view of the interface evolution.

Results and Discussion

Characterization of the TFP electrolyte

Typically, acetonitrile (AN) has the advantages of strong oxidation resistance and high dielectric constant, but it suffers from the limited anti-reduction performance.[37] Therefore, it has been excluded from the main liquid solvent of electrolytes. Since the poor reductive stability of AN, it would be easily reduced by Li metal ($CH_3CN + 2Li \rightarrow CH_3^- + CN^- + 2Li^+$) as shown in Figure S1.[38,39] However, the problem of solvent degradation can be effectively solved by modifying the molecular structure.[40–43] The stability of electrolyte solvents can be achieved by the active α-H atoms replaced with methyl groups. In Figure 1(a), after H of AN is replaced by methyl, due to the absence of acidic hydrogen, PN cannot undergo the electro-chemical reactions that lead to tertiary carbanion. Besides, the introduction of methyl equalizes the charge density distribution of PN molecule, reduces the polarization of the molecule, and improves the reductive stability of the PN. According to the LUMO energy obtained from density functional theory (DFT) simulations, the increase of the LUMO value of PN further indicated that the reduction stability was enhanced (AN:1.01 eV, PN:1.23 eV) as shown in Figure 1(b). Lithium metal stored in TFP electrolyte without corrosion was also viewed as shown in Figure 1(c). Compared with AN, the unique $-CH_3$ group of PN enables it to retain a higher dielectric constant (AN $\varepsilon = 36.0$, PN $\varepsilon = 20.1$)[44] and improve PN's anti-reduction ability at the same time, thus to be more compatible with Li metal.[45]

The electrochemical window is a vital characteristic to evaluate the practicability of as-formed electrolytes. Figure 2(a) shows the LSV curves of TFP electrolytes with different lithium salt concentrations (corresponding to LiTFSI concentrations of 0.5, 1, 2, 4 in FEC/PN (2:3, v%)) and carbonate electrolyte (1 M LiPF$_6$ dissolved in EC/DMC=1:1 v%)). Remarkably, compared with carbonate electrolytes, TFP electrolytes show higher stability in the potential range of 4.0–6.0 V. In the 1 M TFP electrolyte, its oxidation potential reached 4.65 V (vs. Li/Li$^+$), which was higher than that of the carbonate electrolyte (4.09 V). As lithium salt concentration increases, the oxidation potential increases and reaches 5.32 V at 4 M TFP electrolyte. As expected, the electrolyte can stay stable enough against oxidation in the presence of fully methylated PN.

Viscosities (25 °C) of the TFP electrolytes with different LiTFSI concentrations were tested by a cone-plate viscometer (Figure 2b). The viscosities of the TFP electrolytes for 0.5, 1, 2, and 4 M are 3.10, 3.47, 9.30, and 83.28 mPa s, respectively. Commonly, the growth of viscosity results from the increment of electrostatic interactions among the ion pairs, increasing the energy barrier of ion diffusion and leading to a decrease of ionic conductivity. Figure 2(c) shows the ionic conductivity of TFP electrolytes at ambient temperature. As reflected by the viscosity value, the ionic conductivity of 1 M TFP electrolyte (11.53 mS cm^{-1}) is higher than that of other TFP electrolytes (1.09–6.11 mS cm^{-1}). Considerable ionic conductivities make it possible for the rapid plating and stripping of Li metal under high current conditions. Therefore, the 1 M TFP electrolyte was used as the optimal PN-base electrolyte in this work.

As a significant parameter for electrolytes, we have used the method proposed by Abraham et al to detect the Li$^+$ transference number (t_{Li}^+).[46] Higher t_{Li}^+ indicates that the electrolyte has better charge transfer efficiency, which can reduce the concentration polarization of the battery and improve the reversibility of electrode reaction. Figure 2(d) shows that the t_{Li}^+ of the 1 M TFP electrolyte achieves 0.58, which is much higher than that for carbonate electrolyte (0.37, Figure S2). Thus, it is beneficial to eliminate the concentration polarization. According to the Tafel equation, the exchange current density i_0 was further verified with the promising ionic
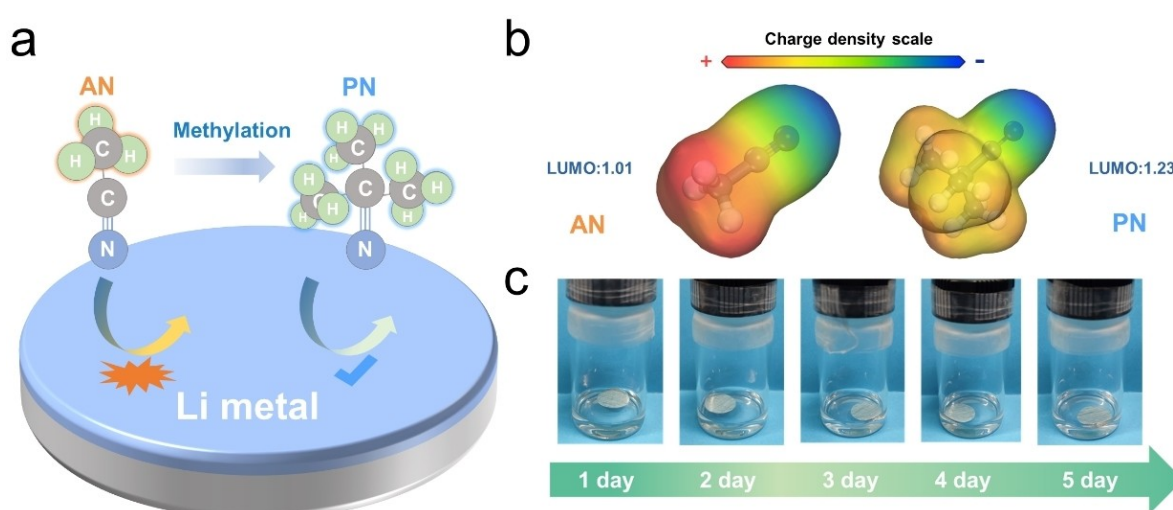

Figure 1. a) Diagram of Li metal stabilization through AN methylation. b) The iso-surface of charge distribution for PN and AN molecule. c) Photos of 1 M TFP electrolyte soaked by lithium-metal foils.
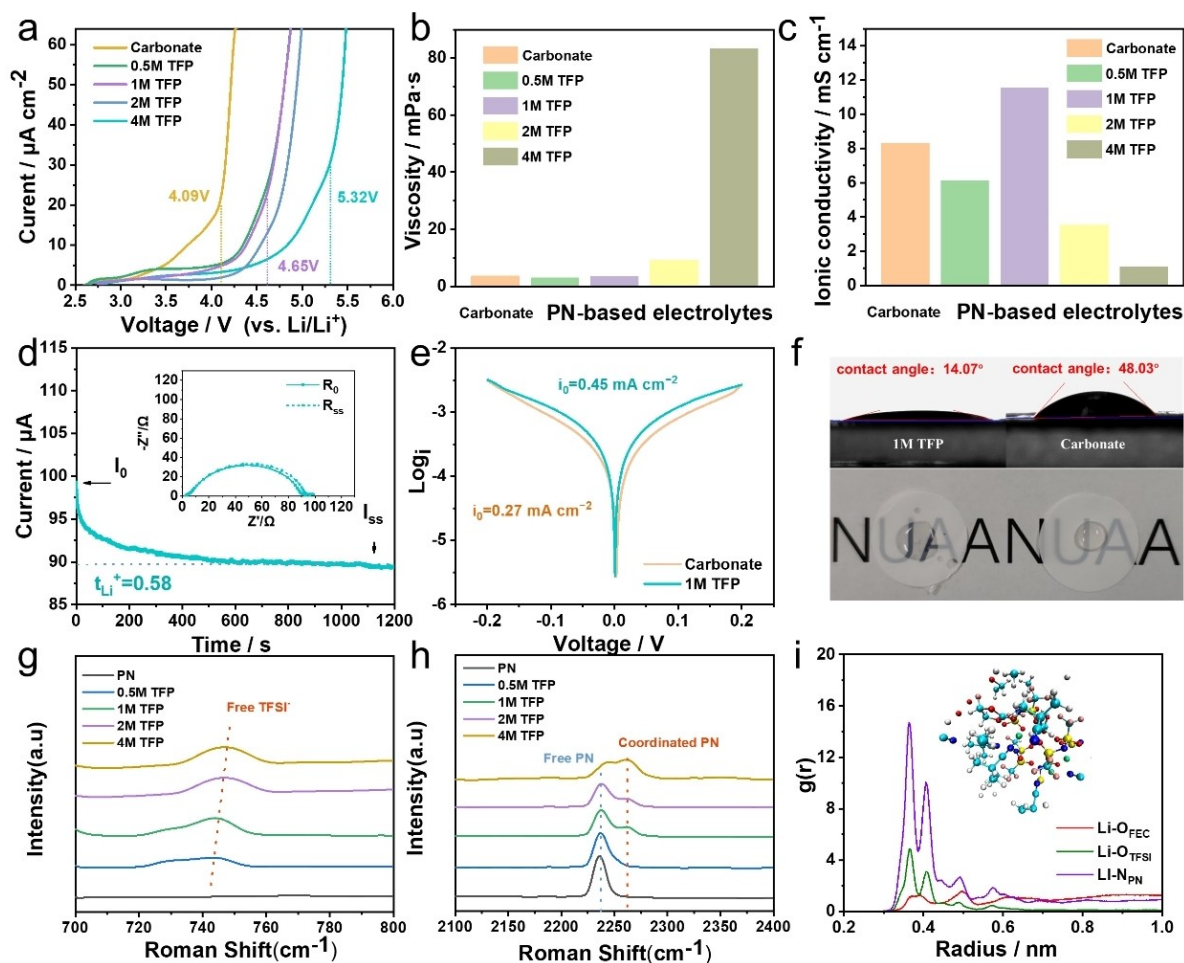
Batteries & Supercaps

Research Article
doi.org/10.1002/batt.202100416

Chemistry
Europe
European Chemical
Societies Publishing

Figure 2. Physical and chemical properties of the electrolyte. a) LSVs of the TFP and carbonate electrolytes, b) viscosities, c) conductivities of the TFP electrolytes, d) the chronoamperometry profile of Li||Li cells in 1 M TFP electrolyte. Resistance change (EIS) before/after potentiostatic perturbation is provided in the inset, e) Tafel curves of Li||Li symmetrical cells, f) contact angle test and diaphragm wettability test of the 1 M TFP and carbonate electrolytes, g and h) Raman spectra of the TFP electrolytes. i) Snapshots of the MD simulation cell and radial distribution function of 1 M TFP electrolyte at 298.15 K (inset shows the distribution of molecules around the Li$^+$ with a radius of 6 nm, C, sky blue; O, red; Li, Green; S, yellow; N, deep blue; H, white, F, pink).

conduction capability of the 1 M TFP electrolyte by plotting logi as a function of overpotential in Figure 2(e). The obtained values of i_0 are 0.27 mA cm^{-2} for the carbonate electrolyte and 0.45 mA cm^{-2} for the 1 M TFP electrolyte, respectively. This suggests a fast charge transfer kinetics and higher reversibility of Li plating/stripping by using TFP electrolyte. The contact angle test shows that 1 M TFP electrolyte has a smaller contact angle of 14.07°, proving the excellent-wetting ability to Li metal. In the wetting experiment of the separator, 1 M TFP electrolyte also shows excellent infiltration to the separator Celgard 2400 (Figure 2f), which can homogeneous the lithium-ion flow and benefit for the uniform deposition.[47]

As known, the —CN group can coordinate with the lithium ion, the highly coordinated Li$^+$-solvent pair of PN was also observed in TFP electrolytes. In Figure 2(g and h), Raman spectra of various electrolytes display that the signal of free PN in the electrolyte decreases gradually (as shown by the —C≡N stretching vibration band at 2236 cm^{-1}) and the signal of solvent combining Li$^+$ and PN increases gradually with the increasing of LiTFSI concentration. The intensity increasement

of the free TFSI$^-$ at 745 cm^{-1} further demonstrates the generation of Li$^+$-coordinated PN (2260 cm^{-1}). In order to further study the solvation structure of TFP electrolyte, a simple molecular dynamics method with the OPLS-AA force field was employed to simulate the electrolyte, as described in Supporting information (Figure S3). The radial distribution function (g(r)) of 1 M TFP electrolyte was calculated using the molecule dynamics (MD) simulation trajectory. The results identify that LiTFSI can coordinate with PN closely (Figure 2i), which is consistent with the Raman spectra result. Because of the higher electro-phobic effect of PN, the higher g(r) value between Li$^+$ and N_{PN} can be concluded that the interactions between Li$^+$ and PN are much stronger than that between Li$^+$ and FEC, which certifies that PN molecules dominates the Li$^+$ coordination. Due to the electron-donating effect of methyl, the desolvation energy barrier of lithium ion is reduced due to the reduced cation binding. Thus, 1 M TFP electrolyte can realize the rapid migration of lithium ions.

Batteries & Supercaps

Research Article
doi.org/10.1002/batt.202100416

Chemistry Europe
European Chemical
Societies Publishing

Lithium-metal anode plating and stripping behavior in the TFP electrolyte

To verify the stability of TFP electrolyte in the cycling process ulteriorly, asymmetric Li||Cu cells were fabricated and tested at different current densities with a capacity of 1 mAh cm^{-2} using 57 μm Li foils (10.7 mAh cm^{-2}, Figure S4). In Figure 3(a), when the current density is 1 mA cm^{-2}, an ascensive CE value of 96.2% can be obtained in the 1 M TFP electrolyte up to 180 cycles, while the CE in the carbonate electrolyte is only 89.4% about 60 cycles. Even improved the current density to 2 mA cm^{-2} in Figure 3(b), the CE of 1 M TFP electrolyte still holds 95.2%, which shows a great improvement compared to the carbonate electrolyte. Remarkably, the increasement of overpotential was significantly inhibited in the 1 M TFP electrolyte (carbonate electrolyte: ~326 mV; 1 M TFP electrolyte: ~72 mV) after 50 cycles. As the number of cycles increases, the overpotential of the Li||Cu in 1 M TFP electrolyte was only ~94 mV as shown in Figure 3(c and d). The high CE and low overpotential using the TFP electrolyte should result from the high electrochemical stability and fast ion transfer through the electrolyte.

Symmetric Li||Li cells were further constructed to evaluate the cycling compatibility of as-optimized electrolyte under the limited capacity of Li metal a current density of 1 mA cm^{-2} (limited capacity of 1 mAh cm^{-2}). As shown in Figure 3(e), cells using the carbonate electrolyte hold a voltage curve with a relatively high voltage hysteresis of ~207 mV at the first cycle and fail rapidly after 200 h due to the dendrite-induced short circuit. This result is highly consistent with the poor CE measured in Li||Cu cells (Figure 3a and b). On the contrary, Li||Li cells exhibit much-improved cycling stability with 1 M TFP electrolyte, together with a relatively low voltage hysteresis of ~60 mV at first cycle and show long-term cyclability up to 500 h. Besides, lower voltage hysteresis was also observed at different current densities for Li||Li cells in the 1 M TFP electrolyte (Figure 3f), suggesting high electrochemical reversibility and compatibility of Li plating/stripping.

Both Li||Cu and Li||Li cells demonstrate excellent cycling stability in the 1 M TFP electrolyte. This property is also synchronously reflected in the electrochemical impedance spectroscopy of Li||Li cells, which reflects the interface phenomenon of Li metal anode (Figure 4a and b). With the increasement of rest time, the impedance of the Li metal in 1 M
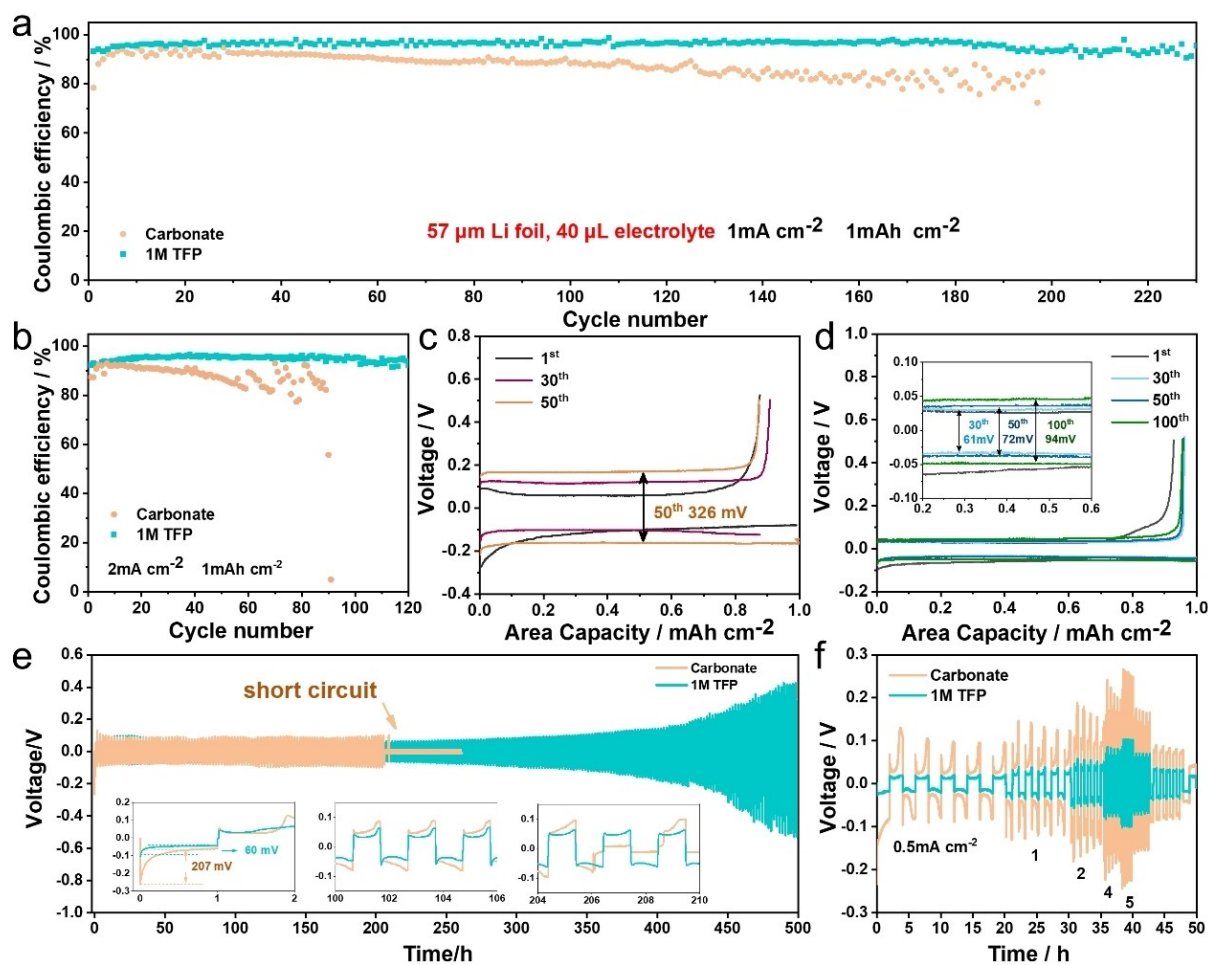

Figure 3. Electrochemical behavior of the electrolytes. Cycling performances of Li||Cu cells at a) 1 mA cm^{-2}, b) 2 mA cm^{-2}, c and d) voltage profiles for Li plating/stripping at 2 mA cm^{-2} in c) carbonate electrolyte and d) 1 M TFP electrolyte, e) Li||Li symmetrical cells using different electrolyte at 1 mA cm^{-2}, f) rate performances of Li||Li cells in 0.5, 1, 2, 4, 5 mA cm^{-2}.
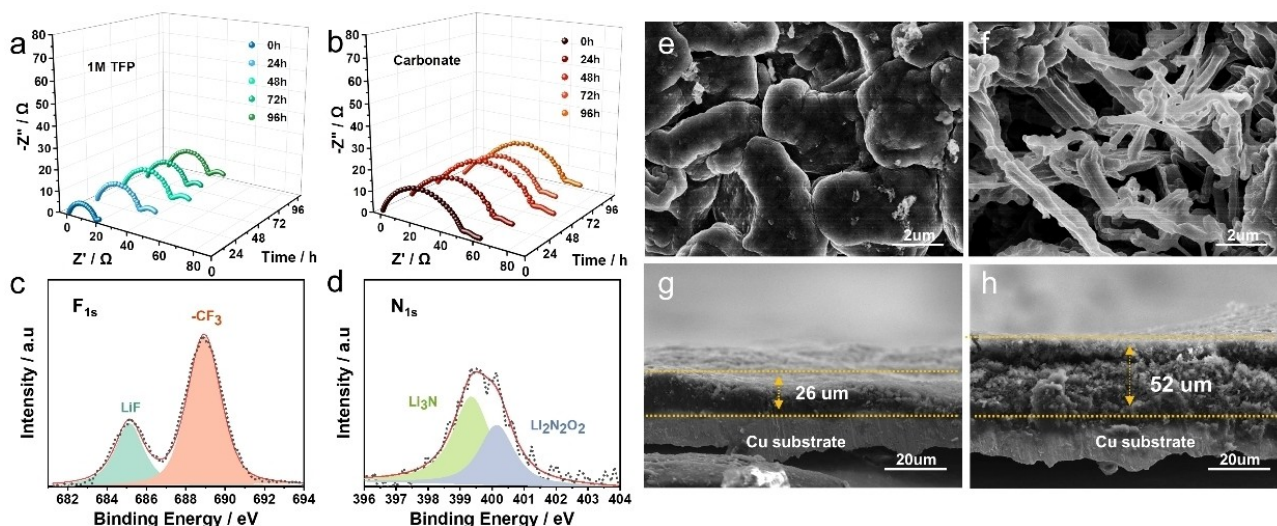
Figure 4. Interfacial properties of Li metal anode. Nyquist plot as a function of standing hours for Li||Li cells in a) 1 M TFP electrolyte; b) carbonate electrolyte, XPS spectra of c) F 1s, d) N 1s, Li surfaces after 100 cycles in the 1 M TFP electrolyte, e, f) SEM images of Li deposition morphology at 1 mA cm^{-2} after 100 cycle e) in the 1 M TFP electrolyte, f) in carbonate electrolyte, g, h) cross-section SEM images of Li deposition morphology at 1 mA cm^{-2} after 100 cycle, g) in the 1 M TFP electrolyte, h) in carbonate electrolyte.

TFP electrolyte held steadily about 35 Ω, which is smaller than that in carbonate electrolyte (53 Ω), and the PN-based electrolyte shows a lower and stable RCT (The detailed fitted values of electrochemical impedance spectroscopy as shown in Figure S5 and Table S1), demonstrating the improvement of interfacial stability of Li metal. These results can be concluded that the 1 M TFP electrolyte can enhance the compatibility between Li metal and electrolyte, as well as forming a satisfying interface.

In order to analyze the reason for better Li performance of cells by using 1 M TFP electrolyte, the surface of Li metal after 100 cycles with 1 M TFP electrolyte was analyzed by X-ray photoelectron spectroscopy (XPS). Compare with SEI formed in carbonate electrolyte (Figure S6), the SEI layer constituted by using the 1 M TFP electrolyte mainly be formed of $-CF_3$, LiF, Li_3N, $Li_2N_2O_2$ as shown in Figure 4(c and d), which is primarily attributed to the interface reactions between PN, TFSI$^-$, FEC, and Li metal. This multi-group interface layer provides promising ionic conductivity, excellent electronic insulation, which inhibits side reactions and improves the performance of durability.[32]

The deposition morphologies (1 mA cm^{-2}, 1 mAh cm^{-2}) of Li onto Cu substrate in different electrolytes were characterized by the field emission scanning electron microscope (FE-SEM). As shown in Figure 4(e), the Li deposited structure with the carbonate electrolyte is porous and loose with many needle-like dendrites. Meanwhile, the thickness of the residual Li on the copper is about 52 μm (Figure 4h). As a comparison, a dendrite-free plating structure is observed by using 1 M TFP electrolyte, bulk Li particle with a few microns can be observed rather than nano dendrites (Figure 4e). The thickness of the residual Li on the copper in the 1 M TFP electrolyte is only about 26 μm (Figure 4g). Such a high-density morphology of Li deposition can alleviate the adverse reactions in the interface of Li metal/electrolyte due to its less contact area with the

electrolyte, leading to high CE and promising plating/stripping stability.

The macroscopic morphology evolution of Li in the electrodeposition process depends on the initial nucleation. To investigate the Li deposition morphology, in situ optical microscopy was employed to characterize the process of Li deposition by a specially designed cell device with a visual window (Figure 5a).[48] The experiment was carried out at a constant current density of 1 mA cm^{-2}. For electrodeposition, according to the Butler-Volmer equation:

$$j = j^0 \exp[-\frac{\alpha nF}{RT}(\varphi - \varphi_e)] - j^0 \exp[-\frac{(1-\alpha)nF}{RT}(\varphi - \varphi_e)]$$

the nucleation barrier can effectively be adjusted by tuning the overpotential of the reduction reaction. A typical lithium deposition potential curve was proposed to study lithium deposition behavior at different potentials. According to the previous work, the driving force of the lithium deposition process can be described to two important characteristics of overpotential: (1) the nucleation overpotential, which drives the nucleation of Li metal, (2) the growth overpotential, which drives Li growth.[49–51] Combined with the plating voltage profile (Figure 5b), the morphological evolution of Li deposition was monitored in situ at the Li||Cu interface, as shown in Figure 5(c and d). Typically, Li initially nucleates on the surface of the copper collector prior to nucleation overpotential. In the carbonate electrolyte (Figure 5c, 0–133 s), Li metal nucleation is concentrated, showing irregular lumpy and mainly concentrated at copper foil surface. In the 1 M TFP electrolyte (Figure 5d, 0–65 s), on account of the promising ionic conductivity (11.53 mS cm^{-1}) and higher lithium-ion transference number, the nucleation sites of Li metal are more uniform and compact. After initial nucleation, the overpotential rises and Li
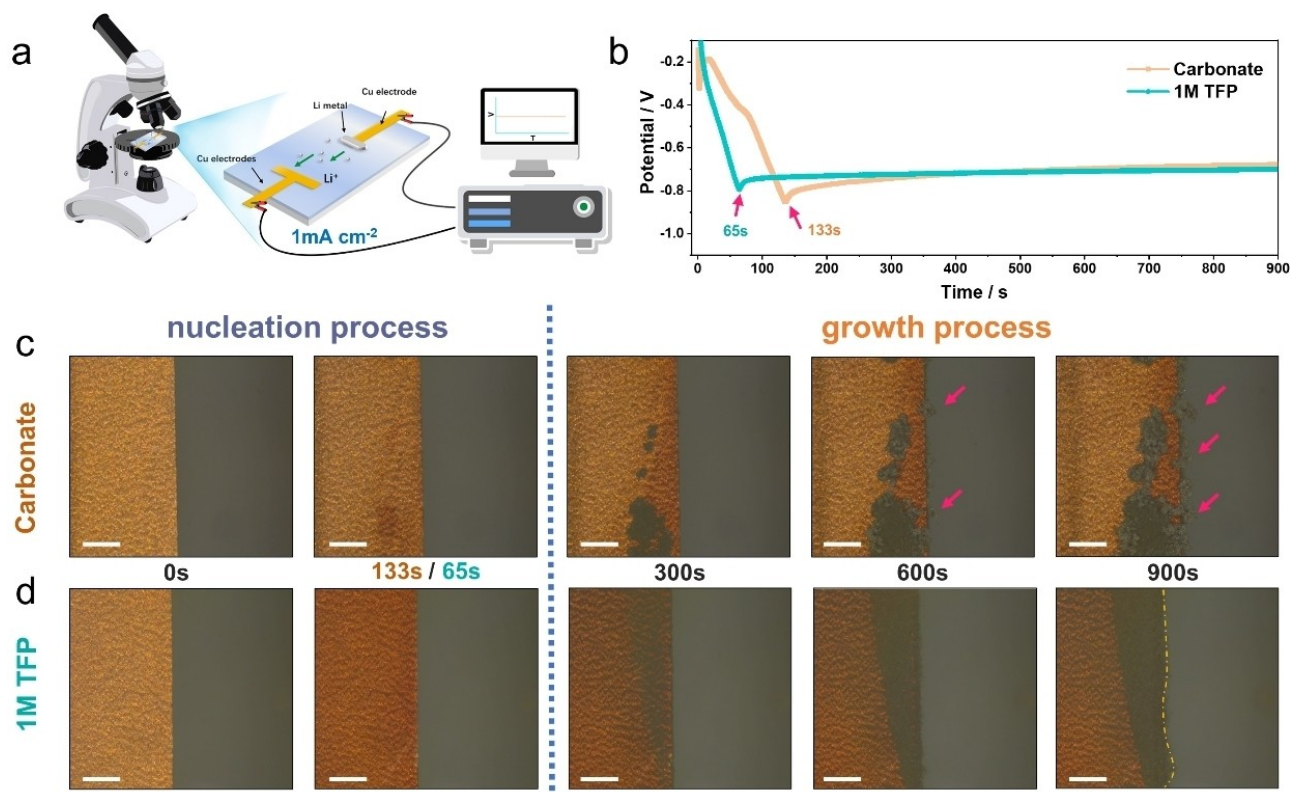
Batteries & Supercaps

Research Article
doi.org/10.1002/batt.202100416

**Chemistry
Europe**
European Chemical
Societies Publishing

Figure 5. In situ characterization of Li metal deposition morphology. a) Diagram of in situ optical microscope observation system. b) The voltage profiles of chronoamperometry. Digital photos of Li metal plating process in c) carbonate electrolyte and d) 1 M TFP electrolyte. Scalebars: 200 μm.

nuclei growth homogeneous, in 1 M TFP electrolyte (Figure 5d, 300–600 s). During the further deposition, the Li propagation still maintains uniform even at the edge of the electrode. On the contrary, a few small and porous Li have been observed in the carbonate electrolyte follow with uncontrolled pulverized Li grows quickly (Figure 5c, 300–600 s). The morphological evolution of Li deposition in these two electrolytes confirms the improvement of the PN on a macroscopic scale, indicating that a denser and more uniform Li deposition is formed in 1 M TFP electrolyte.

Electrochemical behavior of 1 M TFP electrolyte in Li∣∣NCM full cells

Based on the promising plating/stripping stability to Li metal and strong coordination capacity to Ni^{4+}, the effectiveness of the TFP electrolyte is illustrated in Figure 6(a). To further certify the promising resistance to oxidation of the 1 M TFP electrolyte, the Li∣∣NMC622 cells were assembled and long-term cycling performance is compared at 1 C after 0.2 C activation for 3 cycle (loading of active materials ~3.0 mg cm^{-2}) as shown in Figure 6(b). In carbonate electrolyte, although the cells show an approximate initial capacity of 168 mAh g^{-1}, the capacity retention dropped rapidly below 75% after 25 cycles. While the cells using the 1 M TFP electrolyte stably kept capacity retention of 75.3% with a specific capacity of 135 mAh g^{-1} over 300 cycles. The detailed voltage profile of Li∣∣NMC622 full cells

is shown in Figure 6(c and d). Even under the condition of high current density (Figure 6e), the cells with 1 M TFP electrolyte still deliver high charging and discharging capacity and cycling stability, proving the good compatibility and rate capability of 1 M TFP electrolyte in full Li-metal cells.

To further study the electrode/electrolyte interfacial degradation processes, differential electrochemical mass spectrometry (DEMS) was used to quantify the variation of CO_2 under the cell working voltage.[52–55] DEMS system and electrochemical cell internal structure is shown in Figure 7(a and b). As a function of voltage, the corresponding outgassing data show significant differences among different electrolytes. Notably, as the voltage rises in the carbonate electrolyte, the CO_2 gas production gradually rises and reaches a peak at 4.5 V (vs. Li/Li$^+$). This will cause bulging and deformation of the battery, resulting in the degradation of performance. Notably, the suppression of CO_2 evolution up to 4.5 V of 1 M TFP electrolyte, prevents oxidation of the electrolyte and achieves a significant passivation of the interphase. These results not only confirm that TFP electrolyte has high redox stability, but also imply its ability to inhibit side-reactions between electrode and electrolyte during the cycling process.

Conclusion

In summary, a fully methylated pivalonitrile as a stable electrolyte solvent for LMBs is proposed. Substituting methyl for H on

Batteries & Supercaps

Research Article
doi.org/10.1002/batt.202100416

Chemistry Europe
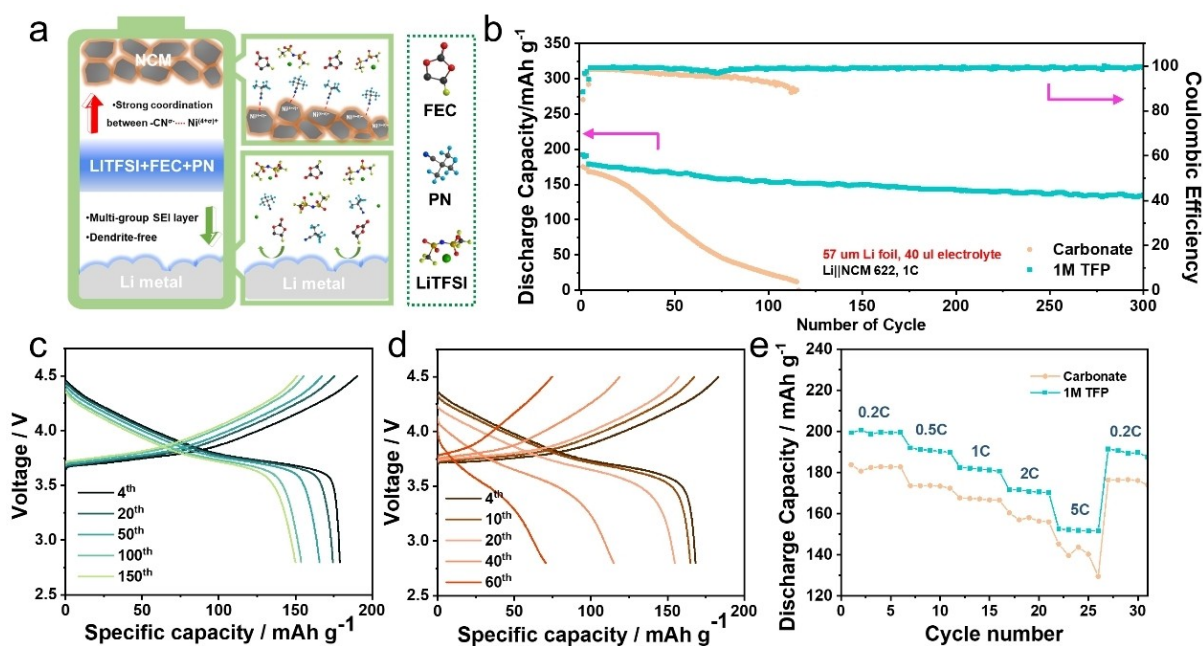European Chemical
Societies Publishing

Figure 6. Electrochemical performance of Li||NCM622. a) Schematic diagram of the effect of TFP electrolyte in the proposed Li||NCM622 cells, b) cycling stability of Li||NMC622 at 1 C (voltage range: 2.8–4.5 V) in different electrolytes. Galvanostatic charge-discharge curves of Li||NMC622 at different cycles in c) carbonate electrolyte d) 1 M TFP electrolyte, e) rate performances at different current densities ranging from 0.2 C to 5 C.
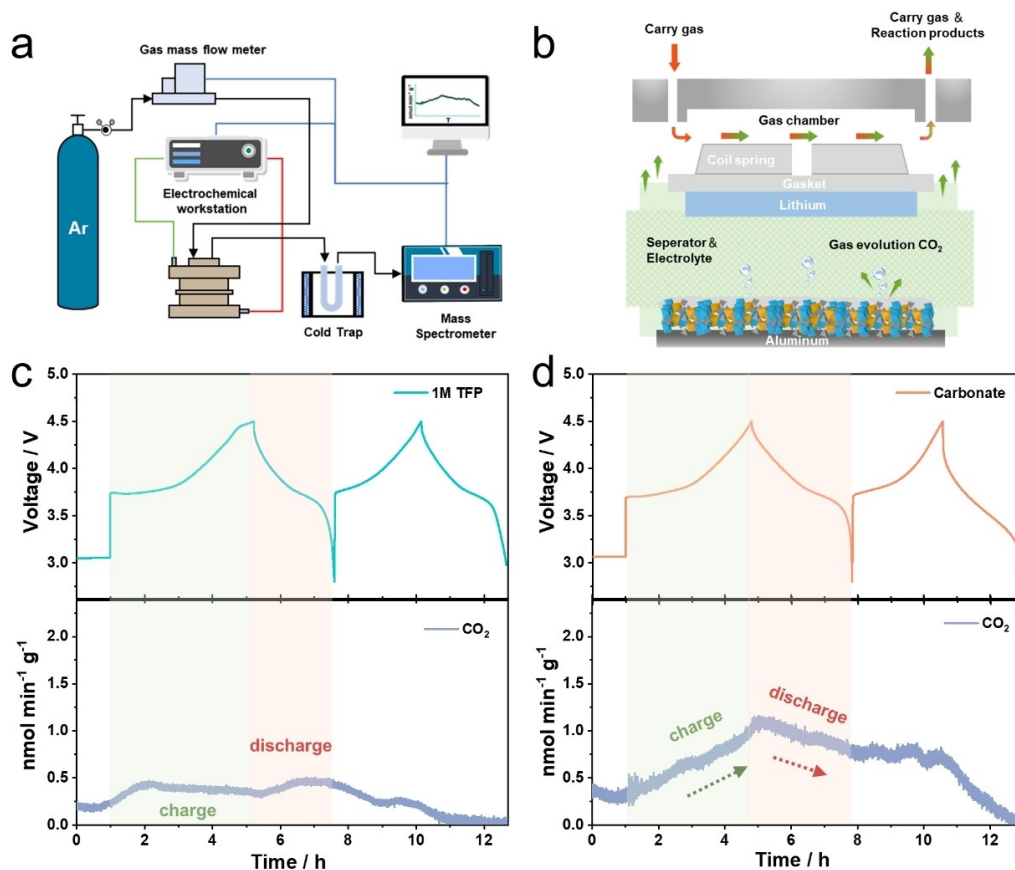

Figure 7. Gas production during the cycle. Schematics of a) the DEMS system, b) the home-made Swagelok type DEMS cell, Rates of carbon dioxide and evolution and voltage profiles in c) 1 M TFP electrolyte or d) carbonate electrolyte.

Batteries & Supercaps

Research Article
doi.org/10.1002/batt.202100416

Chemistry Europe
European Chemical
Societies Publishing

AN significantly improved the reduction stability of nitrile-type electrolytes. The modified hybrid electrolyte reveals low viscosity, high ionic conductivity and lithium transfer numbers. A stable SEI layer could be formed in such a TFP electrolyte. Li deposition process is monitored with in situ optical microscopy, the growth of Li dendrites is suppressed, which improves the stability of the electrode/electrolyte interphase. Consequently, a long-term cyclability can be obtained in Li∥Li cells over 500 h with ultra-thin Li metal. When employed as-optimized TFP electrolyte for high-voltage Li∥NCM622 cells, a high-capacity retention over 75.3% also can be remained after 300 cycles. This work gives light to the design of high-voltage electrolytes for the application of high-energy lithium metal batteries.

Experimental Section

Electrolyte preparation

LiTFSI was obtained from DodoChem and was dried under vacuum overnight in an argon glovebox. FEC (anhydrous, 99.5%, ordered from DodoChem), and pivalonitrile (98% ordered from Sigma-Aldrich) were used with further dehydration. The moisture content in the electrolytes was less than 10 ppm. All electrolytes were prepared in an argon glovebox ($H_2O < 0.1$ ppm, $O_2 < 0.1$ ppm). PN-based electrolytes were prepared simply by mixing PN and FEC additive in the presence of different contents of LiTFSI salt in the argon-filled glovebox and stirring at 25 °C.

Battery fabrication

Coin cell assembly was carried out in an argon-filled glovebox by using coin cell 2016 type. The volume of the electrolyte in a coin cell was 40 μL and utilized a single piece of Celgard 2400 separator. Lithium metal foil was first rolled to control the thickness of the lithium sheet while removing any impurities from the surface. A Land Instruments Battery Tester was used for the cells. The electrochemical stability was determined by linear sweep voltammetry (LSV) on a Biologic electrochemical workstation. With a scanning rate of 10 mV s^{-1} from open-circuit voltage to 6 V at room temperature.

in-situ Optical microscopy

We designed an ultra-thin lithium metal transparent battery, using copper foil and lithium foil as working electrodes and counter electrodes. The two electrodes were aligned in parallel with a gap. The in-situ observation of the Li depositing process was conducted with an optical microscope and ChenHua CHI660 system.

DEMS measuring system

The DEMS system was built in-house. It was based on a commercial quadrupole mass spectrometer and a home-made Swagelok type DEMS cell with two PEEK capillary tubes as purge gas inlet and outlet. The flow rate of purge gas was controlled by a digital mass flow meter (Bronkhorst). The details of the purging system and the DEMS cell were shown in Figure 7(a and b). 3 mL min^{-1} of high purity Ar was used as a carrier gas and acted as the internal tracer gas with known invariable flux. The DEMS cell was controlled by a LAND CT2001 A battery testing system.

Supporting Information

Supporting Information is available from the Wiley Online Library or from the author.

Conflict of Interest

The authors declare no conflict of interest.

Data Availability Statement

The data that support the findings of this study are openly available in Batteries & Supercaps at https://doi.org/[10.1002], reference number 55.

[1] M. Armand, J. M. Tarascon, *Nature* **2008**, *451*, 652–657.
[2] J. W. Choi, D. Aurbach, *Nat. Rev. Mater.* **2016**, *1*, 16013.
[3] S. Fang, D. Bresser, S. Passerini, *Adv. Energy Mater.* **2020**, *10*, 1902485.
[4] L. P. Wang, Z. R. Wu, J. Zou, P. Gao, X. B. Niu, H. Li, L. Q. Chen, *Joule* **2019**, *3*, 2086–2102.
[5] L. F. Nazar, G. Goward, F. Leroux, M. Duncan, H. Huang, T. Kerr, J. Gaubicher, *Int. J. Inorg. Mater.* **2001**, *3*, 191–200.
[6] D. C. Lin, Y. Y. Liu, Y. Cui, *Nat. Nanotechnol.* **2017**, *12*, 194–206.
[7] Y. M. Sun, N. A. Liu, Y. Cui, *Nat. Energy* **2016**, *1*, 16071.
[8] Y. Zhang, T. T. Zuo, J. Popovic, K. Lim, Y. X. Yin, J. Maier, Y. G. Guo, *Mater. Today* **2020**, *33*, 56–74.
[9] P. Shi, X. B. Cheng, T. Li, R. Zhang, H. Liu, C. Yan, X. Q. Zhang, J. Q. Huang, Q. Zhang, *Adv. Mater.* **2019**, *31*, 1902785.
[10] J. B. Goodenough, Y. Kim, *Chem. Mater.* **2010**, *22*, 587–603.
[11] K. Xu, *Chem. Rev.* **2014**, *114*, 11503–11618.
[12] D. Zhou, R. L. Liu, Y. B. He, F. Y. Li, M. Liu, B. H. Li, Q. H. Yang, Q. Cai, F. Y. Kang, *Adv. Energy Mater.* **2016**, *6*, 1502214.
[13] X. Liang, Q. Pang, I. R. Kochetkov, M. S. Sempere, H. Huang, X. Q. Sun, L. F. Nazar, *Nat. Energy* **2017**, *2*, 17119.
[14] Y. Z. Li, Y. B. Li, A. L. Pei, K. Yan, Y. M. Sun, C. L. Wu, L. M. Joubert, R. Chin, A. L. Koh, Y. Yu, J. Perrino, B. Butz, S. Chu, Y. Cui, *Science* **2017**, *358*, 506–510.
[15] X. B. Cheng, R. Zhang, C. Z. Zhao, Q. Zhang, *Chem. Rev.* **2017**, *117*, 10403–10473.
[16] L. Xu, J. Yang, M. Huang, L. Pi, K. Du, D. Wang, A. Lin, C. Peng, *Chem. Eng. J.* **2021**, *419*, 129494.
[17] E. Markevich, G. Salitra, P. Hartmann, J. Kulisch, D. Aurbach, K. J. Park, C. S. Yoon, Y. K. Sun, *J. Electrochem. Soc.* **2019**, *166*, A5265–A5274.
[18] J. H. Kim, S. J. Kim, T. Yuk, J. Kim, C. S. Yoon, Y. K. Sun, *ACS Energy Lett.* **2018**, *3*, 3002–3007.
[19] X. L. Fan, C. S. Wang, *Chem. Soc. Rev.* **2021**, *50*, 10486–10566.
[20] H. Z. Zhi, L. D. Xing, X. W. Zheng, K. Xu, W. S. Li, *J. Phys. Chem. Lett.* **2017**, *8*, 6048–6052.

Batteries & Supercaps

Research Article
doi.org/10.1002/batt.202100416

Chemistry Europe
European Chemical
Societies Publishing

[21] H. C. Yang, J. Li, Z. H. Sun, R. P. Fang, D. W. Wang, K. He, H. M. Cheng, F. Li, *Energy Storage Mater.* **2020**, *30*, 113–129.

[22] Z. L. Hu, G. J. Li, A. X. Wang, J. Y. Luo, X. J. Liu, *Batteries & Supercaps* **2020**, *3*, 331–335.

[23] F. Q. Liu, W. P. Wang, Y. X. Yin, S. F. Zhang, J. L. Shi, L. Wang, X. D. Zhang, Y. Zheng, J. J. Zhou, L. Li, Y. G. Guo, *Sci. Adv.* **2018**, *4*, eaat5383.

[24] S. H. Jiao, X. D. Ren, R. G. Cao, M. H. Engelhard, Y. Z. Liu, D. H. Hu, D. H. Mei, J. M. Zheng, W. G. Zhao, Q. Y. Li, N. Liu, B. D. Adams, C. Ma, J. Liu, J. G. Zhang, W. Xu, *Nat. Energy* **2018**, *3*, 739–746.

[25] X. L. Fan, L. Chen, O. Borodin, X. Ji, J. Chen, S. Hou, T. Deng, J. Zheng, C. Y. Yang, S. C. Liou, K. Amine, K. Xu, C. S. Wang, *Nat. Nanotechnol.* **2018**, *13*, 1191–1191.

[26] X. L. Fan, X. Ji, L. Chen, J. Chen, T. Deng, F. D. Han, J. Yue, N. Piao, R. X. Wang, X. Q. Zhou, X. Z. Xiao, L. X. Chen, C. S. Wang, *Nat. Energy* **2019**, *4*, 882–890.

[27] Y. Y. C. Yang, D. M. Davies, Y. J. Yin, O. Borodin, J. Z. Lee, C. C. Fang, M. Olguin, Y. H. Zhang, E. S. Sablina, X. F. Wang, C. S. Rustomji, Y. S. Meng, *Joule* **2019**, *3* 1986–2000.

[28] P. Jaumaux, Q. Liu, D. Zhou, X. F. Xu, T. Y. Wang, Y. Z. Wang, F. Y. Kang, B. H. Li, G. X. Wang, *Angew. Chem. Int. Ed.* **2020**, *59*, 9134–9142; *Angew. Chem.* **2020**, *132*, 9219–9227.

[29] W. J. Xue, Z. Shi, M. J. Huang, S. T. Feng, C. Wang, F. Wang, J. Lopez, B. Qiao, G. Y. Xu, W. X. Zhang, Y. H. Dong, R. Gao, Y. Shao-Horn, J. A. Johnson, J. Li, *Energy Environ. Sci.* **2020**, *13*, 212–220.

[30] X. D. Ren, S. R. Chen, H. Lee, D. H. Mei, M. H. Engelhard, S. D. Burton, W. G. Zhao, J. M. Zheng, Q. Y. Li, M. S. Ding, M. Schroeder, J. Alvarado, K. Xu, Y. S. Meng, J. Liu, J. G. Zhang, W. Xu, *Chem.* **2018**, *4*, 1877–1892.

[31] Q. Wang, Z. Yao, C. Zhao, T. Verhallen, D. P. Tabor, M. Liu, F. Ooms, F. Kang, A. Aspuru-Guzik, Y.-S. Hu, M. Wagemaker, B. Li, *Nat. Commun.* **2020**, *11*, 4188.

[32] Z. Hu, F. Xian, Z. Guo, C. Lu, X. Du, X. Cheng, S. Zhang, S. Dong, G. Cui, L. Chen, *Chem. Mater.* **2020**, *32*, 3405–3413.

[33] C. Fu, Y. Ma, S. Lou, C. Cui, L. Xiang, W. Zhao, P. Zuo, J. Wang, Y. Gao, G. Yin, *J. Mater. Chem. A* **2020**, *8*, 2066–2073.

[34] K. P. Ho, K. Ho, R. Wang, Y. Xu, W. C. Luk, M. M. Hsu, United States Patent. No.9666906, **2015**.

[35] Z. Peng, X. Cao, P. Y. Gao, H. P. Jia, X. D. Ren, S. Roy, Z. D. Li, Y. Zhu, W. P. Xie, D. Y. Liu, Q. Y. Li, D. Y. Wang, W. Xu, J. G. Zhang, *Adv. Funct. Mater.* **2020**, *30*, 2001285.

[36] P. J. Alarco, Y. Abu-Lebdeh, A. Abouimrane, M. Armand, *Nat. Mater.* **2004**, *3*, 476–481.

[37] N. D. Trinh, D. Lepage, D. Ayme-Perrot, A. Badia, M. Dolle, D. Rochefort, *Angew. Chem. Int. Ed.* **2018**, *57*, 5072–5075; *Angew. Chem.* **2018**, *130*, 5166–5169.

[38] Y. Yamada, K. Furukawa, K. Sodeyama, K. Kikuchi, M. Yaegashi, Y. Tateyama, A. Yamada, *J. Am. Chem. Soc.* **2014**, *136*, 5039–5046.

[39] M. W. Rupich, L. Pitts, K. M. Abraham, *J. Electrochem. Soc.* **1982**, *129*, 1857.

[40] Z. C. Zhang, J. Lu, R. S. Assary, P. Du, H. H. Wang, Y. K. Sun, Y. Qin, K. C. Lau, J. Greeley, P. C. Redfern, H. Iddir, L. A. Curtiss, K. Amine, *J. Phys. Chem. C* **2011**, *115*, 25535–25542.

[41] Z. M. Huang, H. P. Zeng, M. L. Xie, X. Lin, Z. M. Huang, Y. Shen, Y. H. Huang, *Angew. Chem. Int. Ed.* **2019**, *58*, 2345–2349; *Angew. Chem.* **2019**, *131*, 2367–2371.

[42] B. D. Adams, R. Black, Z. Williams, R. Fernandes, M. Cuisinier, E. J. Berg, P. Novak, G. K. Murphy, L. F. Nazar, *Adv. Energy Mater.* **2015**, *5*, 1400867.

[43] Z. Yu, H. S. Wang, X. Kong, W. Huang, Y. C. Tsao, D. G. Mackanic, K. C. Wang, X. C. Wang, W. X. Huang, S. Choudhury, Y. Zheng, C. V. Amanchukwu, S. T. Hung, Y. T. Ma, E. G. Lomeli, J. Qin, Y. Cui, Z. N. Bao, *Nat. Energy* **2020**, *5*, 526–533.

[44] V. S. Bryantsev, V. Uddin, V. Giordani, W. Walker, D. Addison, G. V. Chase, *J. Electrochem. Soc.* **2013**, *160*, A160–A171.

[45] J. Alvarado, M. A. Schroeder, T. P. Pollard, X. Wang, J. Z. Lee, M. Zhang, T. Wynn, M. Ding, O. Borodin, Y. S. Meng, K. Xu, *Energ Environ. Sci.* **2019**, *12*, 780–794.

[46] K. M. Abraham, Z. Jiang, B. Carroll, *Chem. Mater.* **1997**, *9*, 1978–1988.

[47] X. F. He, X. Liu, Q. Han, P. Zhang, X. S. Song, Y. Zhao, *Angew. Chem. Int. Ed.* **2020**, *59*, 6397–6405; *Angew. Chem.* **2020**, *132*, 6459–6467.

[48] Z. W. Li, L. Y. Wu, S. Y. Dong, T. Z. Xu, S. P. Li, Y. F. An, J. M. Jiang, X. G. Zhang, *Adv. Funct. Mater.* **2020**, *31*, 2006495.

[49] R. Winand, *J. Appl. Electrochem.* **1991**, *21*, 377–385.

[50] A. Pei, G. Y. Zheng, F. F. Shi, Y. Z. Li, Y. Cui, *Nano Lett.* **2017**, *17*, 1132–1139.

[51] W. Plieth, *Science* **2008**, 291–321.

[52] S. E. Renfrew, B. D. McCloskey, *ACS Appl. Energ. Mater.* **2019**, *2*, 3762–3772.

[53] J. Sicklinger, M. Metzger, H. Beyer, D. Pritzl, H. A. Gasteiger, *J. Electrochem. Soc.* **2019**, *166*, A2322–A2335.

[54] S. E. Renfrew, B. D. McCloskey, *J. Am. Chem. Soc.* **2017**, *139*, 17853–17860.

[55] B. Zhou, L. M. Guo, Y. T. Zhang, J. W. Wang, L. P. Ma, W. H. Zhang, Z. W. Fu, Z. Q. Peng, *Adv. Mater.* **2017**, *29*, 1701568.